

Mass Flows in Cometary UCHII Regions

Qing-Feng Zhu¹, John H. Lacy¹, Daniel T. Jaffe¹

Astronomy Department, University of Texas at Austin, Austin, TX 78712

`zhuqf@astro.as.utexas.edu`

and

Thomas K. Greathouse¹

Lunar and Planetary Institute, 3600 Bay Area Boulevard, Houston, TX 77058-1113

and

Matthew J. Richter¹

Department of Physics, University of California, Davis, CA 95616-8677

ABSTRACT

High spectral and spatial resolution, mid-infrared fine structure line observations toward two ultracompact HII (UCHII) regions (G29.96 -0.02 and Mon R2) allow us to study the structure and kinematics of cometary UCHII regions. In our earlier study of Mon R2, we showed that highly organized mass motions accounted for most of the velocity structure in that UCHII region. In this work, we show that the kinematics in both Mon R2 and G29.96 are consistent with motion along an approximately paraboloidal shell. We model the velocity structure seen in our mapping data and test the stellar wind bow shock model for such paraboloidal like flows. The observations and the simulation indicate that the ram pressures of the stellar wind and ambient interstellar medium cause the accumulated mass in the bow shock to flow along the surface of the shock. A relaxation code reproduces the mass flow's velocity structure as derived by the

¹Visiting Astronomer at the Infrared Telescope Facility, which is operated by the University of Hawaii under Cooperative Agreement no. NCC 5-538 with the National Aeronautics and Space Administration, Office of Space Science, Planetary Astronomy Program.

analytical solution. It further predicts that the pressure gradient along the flow can accelerate ionized gas to a speed higher than that of the moving star. In the original bow shock model, the star speed relative to the ambient medium was considered to be the exit speed of ionized gas in the shell.

Subject headings: interstellar medium - ultracompact H II regions - G29.96 -0.02
- Mon R2 IRS1

1. Introduction

Ultracompact HII (UCHII) regions form when massive OB stars ignite inside dense molecular clouds and high energy UV photons ionize the surrounding neutral material. They have small sizes ($\lesssim 0.1$ pc), high electron densities ($\gtrsim 10^4$ cm $^{-3}$), and high emission measures ($EM = \int n_i n_e dl \gtrsim 10^7$ pc cm $^{-6}$) (Wood & Churchwell 1989b). The ionization increases the temperature ($\sim 10^4$ K) and number density ($H_2 \rightarrow 2p^+ + 2e^-$) causing the gas pressure inside the regions to be at least two orders of magnitude higher than in the surrounding molecular gas. UCHII regions should then expand at approximately the speed of sound in the ionized gas (~ 10 km s $^{-1}$) until they reach pressure equilibrium with the surrounding material or break out of their parent molecular clouds. Because of this expansion, the density and emission measure both should drop with time. Once the emission measure drops below 10^7 pc cm $^{-6}$, these HII regions will no longer be considered ultracompact.

A longstanding puzzle regarding UCHII regions involves their numbers and their lifetimes. If HII regions expand at 10 km s $^{-1}$, they should remain ultracompact for only $\sim 10^4$ yr. Since this is $<1\%$ of the lifetime of an OB star, the number of UCHII regions should be $<1\%$ the number of OB stars. Radio interferometry observations confirm that the ratio of IRAS far-infrared (FIR) flux densities provides an efficient way to select embedded OB stars from the IRAS data (Wood & Churchwell 1989b; Churchwell 1990; Garay et al. 1993; Kurtz et al. 1994; Miralles et al. 1994). However, counts of IRAS FIR sources with the spectral characteristics of UCHII regions and the optically visible O stars in the solar neighborhood show that OB stars spend $\sim 10 - 20\%$ of their main-sequence lifetime embedded in molecular clouds (Wood & Churchwell 1989a). Apparently, the lifetimes of UCHII regions are an order of magnitude larger than predicted by the classical pressure-driven spherical expansion model.

The variety of observed UCHII morphologies, including spherical, shell-like, cometary, and irregular, also needs to be explained. An understanding of the kinematics of the ionized gas will help provide an explanation of both the morphologies and the lifetime of UCHII regions. It has been suggested that long lifetimes could result from some kind of containment

or gas replenishment mechanism (Hollenbach et al. 1994; Dyson et al. 1995; Redman et al. 1996; Williams et al. 1996; Redman et al. 1998). Various mechanisms would have different effects on the morphologies and the kinematics of UCHII region, suggesting that observations could distinguish between these mechanisms.

The well-organized overall appearance of cometary UCHII regions make them good objects in which to study UCHII region kinematics and morphology. One way to explain these objects is with a bow shock model, which suggests the cometary structure of some UCHII regions is the result of the supersonic motion of OB stars with high speed winds through molecular clouds (Hughes & Viner 1976; Wood & Churchwell 1989b; van Buren et al. 1990; Mac Low et al. 1991; van Buren & Mac Low 1992). Swept-up ambient gas and stellar wind material accumulate where the ram pressures associated with these two mass flows balance, resulting in a shell-like structure and a surface flow. This model may not explain the lifetime of all UCHII regions, but could provide a part of the solution to this problem.

Because ultracompact HII regions are formed inside dense molecular clouds, the extinction toward these objects usually is very high, with a typical line of sight extinction of $A_v = 30 - 50$ (Hanson et al. 2002). Thus, optical techniques used in diffuse HII region observations are inappropriate for studies of UCHII regions. Low extinction at infrared and radio wavelengths makes these wavelength bands more suitable for studies of UCHII regions. Hydrogen radio recombination line observations toward UCHII regions have been carried out extensively (Garay et al. 1985; Kim & Koo 2001; Araya et al. 2002). These observations reveal that thermal motions cannot account for the linewidths of many UCHII regions. However, significant thermal broadening makes it hard to study the velocity structure in these regions using hydrogen recombination lines because of hydrogen’s low atomic mass (Jaffe & Martín-Pintado 1999; Sewilo et al. 2004; De Pree et al. 2004, and references therein). The thermal line width of hydrogen recombination lines is $\Delta v_{FWHM} \simeq 21.4 \text{ km s}^{-1}$ for gas with a temperature of 10^4 K . This large thermal linewidth means that heavier ions are better probes of bulk motion; the thermal broadening is only about 4.8 km s^{-1} for Ne^+ ions at the same temperature. Mid-infrared ionic fine-structure lines have been used to probe the structure and excitation of HII regions (Beck et al. 1981; Lacy et al. 1982; Takahashi et al. 2000), but generally with too low spectral resolution to study gas motions. To study kinematics and distinguish organized motions from turbulence and thermal broadening of heavy ions, one needs $\simeq 5 \text{ km s}^{-1}$ velocity resolution.

We have begun a program of high spectral resolution observations of mid-infrared fine structure line emission from UCHII regions. By mapping a small sample of UCHII regions of different morphologies at high spatial resolution in $[Ne \text{ II}]\lambda 12.8 \mu\text{m}$, $[Ar \text{ III}]\lambda 9.0 \mu\text{m}$,

[S III] λ 18.7 μ m and [S IV] λ 10.5 μ m, we can study the kinematics and physical conditions in UCHII regions in order to better understand massive star formation and the relationship between these stars and their surrounding environments. Among these lines, the [Ne II] line is particularly bright and is present in HII regions with a broad range of excitation, so it is well suited for kinematic analysis. We presented high spectral resolution observations of one cometary UCHII region, Mon R2 IRS1 (Mon R2 hereafter), in Jaffe et al. (2003). In the current paper, we present [Ne II] observations of another cometary UCHII region, G29.96 - 0.02 (G29.96 hereafter). We also examine bow shock models in some detail and compare them to the observations of both G29.96 and Mon R2.

In section 2, we describe our mapping and data reduction methods. We present our [Ne II] line emission observations toward G29.96 in section 3. In section 4, we describe the kinematics of the bow shock model and our relaxation method for simulating the formation of the surface flow. We also introduce an additional acceleration, due to the pressure gradient in the ionized gas along the flow. In section 5, we compare the model predictions with the [Ne II] observations of G29.96 and Mon R2. Finally, we discuss the existing problems of models for cometary UCHII regions in section 6.

2. Observations

2.1. Instrument

The [Ne II] observations of G29.96 were carried out with TEXES (the Texas Echelon Cross Echelle Spectrograph, Lacy et al. 2002) on the NASA 3 meter Infrared Telescope Facility (IRTF) on Mauna Kea, in June, 2001. TEXES is a high resolution ($R \leq 100,000$) spectrograph operating at mid-infrared (5-25 μ m) wavelengths. The slit, with a 1.4'' width and a 11.5'' length, was oriented north-south on the sky. With this slit, we achieved a spectral resolution of $\sim 4 \text{ km s}^{-1}$ or $R = 75,000$ at 12.8 μ m. Each pixel along the slit was about 0.36'' on the sky, which is a little smaller than half of the diffraction limit (0.88'') of the IRTF at 12.8 μ m. To map the regions of interest we stepped the telescope west to east across the objects without chopping. Multiple, partially overlapping scans were needed to cover the entire region. For G29.96, each scan had a length of 20'' with a step size of 0.4''. For Mon R2, each scan was 45'' long with 0.7'' steps (Jaffe et al. 2003). Nine overlapping scans were made on G29.96, and 20 scans were made on Mon R2. Because the scans overlapped, the integration time at each point in the map is approximately 18 seconds for G29.96 and 8 seconds for Mon R2.

2.2. Data Reduction

The spectral-spatial datacubes produced from the scans were first reduced with a custom Fortran reduction program that performs general purpose corrections, such as the correction of optical distortions, flat fielding, bad pixel masking and cosmic ray spike removal (Lacy et al. 2002). Radiometric calibration was obtained from measurements of an ambient temperature blackbody before each set of scans, giving intensities in units of $\text{erg cm}^{-2} \text{s}^{-1} \text{sr}^{-1} (\text{cm}^{-1})^{-1}$. The uncertainties in the intensity are mostly systematic, and are probably $\sim \pm 20\%$. The wavelength calibration was obtained from sky emission lines, and is accurate to $\sim 1 \text{ km s}^{-1}$. IDL scripts were used to do the sky background subtraction, multiple scan cross-correlation and combining, and datacube manipulation. Positions safely off the object at both ends of each scan allow us to interpolate the sky emission at each step position. In doing the sky background subtraction, we assumed that the sky background varies linearly with time during the course of a scan, based on the brightness of pixels off the object. After sky emission subtraction, multiple scans of the same region were cross-correlated, shifted, and added to make a complete datacube for the object.

3. Results

We show the integrated [Ne II] line emission map for G29.96 in Fig. 1. The overall cometary shape is apparent and is symmetric about an axis at a position angle $\sim 70^\circ$ east of north. The brightest emission forms an arc perpendicular to the symmetry axis. To the west of the arc, the line emission drops rapidly from the peak value to the background level within $4''$. On the east side of the bright arc, fainter emission extends over $13''$ to the east-northeast. The change of the emission level is much more gradual and less uniform. The east edge of the region is much fuzzier and broken by a faint “lane” into two parts. The southern portion extends the curve of the emission arc out $\sim 6''$ and ends at a clump of ionized gas of size $\sim 3'' \times 3''$. From our velocity channel maps (Fig. 2), we can see that it is the continuous extension of the arc.

Velocity channel maps of G29.96 (Fig. 2) show additional details. A cavity is present at medium and lower velocity channels, from $\sim 82 \text{ km s}^{-1}$ to $\sim 94 \text{ km s}^{-1}$. The fainter structures on the east side of the region and the brighter arc form an almost complete ring around the cavity, although the symmetry axis of the elliptical ring is at a somewhat larger position angle ($\sim 120^\circ$) than that of the bright arc ($\sim 70^\circ$). A similar ring is seen in channel maps of Mon R2 (Jaffe et al. 2003), except that the major axis of the ring in Mon R2 is nearly perpendicular to the symmetry axis of its bright arc. A compact emission peak centered at $V_{LSR} \sim 108 \text{ km s}^{-1}$ can be seen $\sim 5''$ northeast of the peak of the arc in G29.96. The [Ne II]

line is generally broad, reaching $\sim 40 \text{ km s}^{-1}$ near the bright arc. The emission is typically bright near the velocity of the ambient cloud ($V_{LSR} \sim 98 \text{ km s}^{-1}$, obtained from single dish observations of rotational transitions of CS molecules, Martín-Hernández et al. 2003, and references therein), but the line is significantly blueshifted ahead of the emission peak. The line center reaches a $V_{LSR} \sim 82 \text{ km s}^{-1}$ at the west edge of the region

In Fig. 3, we plot [Ne II] line contours on the top of the VLA 2 cm continuum image of G29.96 (Fey et al. 1995). We first aligned the two maps, assuming they are emitted by the same ionized gas. We then convolved the radio map with our beam. The close resemblance of the maps after convolution suggests that the much sharper edges seen in the VLA image are the result of its higher spatial resolution ($< 0.56''$). Comparing a cross-cut along the symmetry axis (Fig. 4) confirms that [Ne II] and radio free-free flux are both proportional to the emission measure of the region. Radio recombination line observations at $0.62''$ and 4 km s^{-1} resolution showed similar arc-like structure (Wood & Churchwell 1991). They also showed that the H76 α line is broader in front of the radio continuum emission arc, where the velocity gradient is also the highest.

Martín-Hernández et al. (2003) obtained a narrow-band H₂ 1-0 S(1) filter map and K band ($2.07 - 2.19 \mu\text{m}$) spectra of the region with a resolution of $R=8,000$ along a $120''$ long slit along the symmetry axis. Their map shows many local near-infrared emission clumps together with the proposed ionizing star of the region lying $\sim 2''.3$ northeast ($p.a. = 64^\circ$) of the emission peak. We mark the star position with an asterisk in our map according to this offset (Fig. 1). Their $Br\gamma$ linewidth ranges between $\sim 42 \text{ km s}^{-1}$ and $\sim 62 \text{ km s}^{-1}$ and shows significant blueshift in front of the emission arc, which is consistent with our [Ne II] observations. The fact that $Br\gamma$ line is systematically broader than [Ne II] along the slit supports the idea that [Ne II] is a better tracer of the ionized gas motions.

4. Bow Shock and Relaxation - A Physical Model for Parabolic Flow

In this section, we present an extension of the analytic solution for bow shocks using a numerical relaxation technique. We then use the resulting gas flow as a template with which we can compare the observed kinematics of G29.96 and Mon R2.

4.1. Analytical Solution

Bow shock models have been explored to explain the formation of cometary UCHII regions by several authors (van Buren et al. 1990; Mac Low et al. 1991; van Buren & Mac

Low 1992; Wilkin 1996). They describe a situation where a star with a strong stellar wind and high UV luminosity moves inside a dense molecular cloud. In the frame of reference of the star, the stellar wind and ambient material collide and create a stationary shock region approximately paraboloidal in shape in front of the star. The standoff distance r_0 is determined by pressure balance at the apex of the shell:

$$\rho_w v_w^2 + n_w k T_w = \rho_a v_*^2 + n_a k T_a, \quad (1)$$

where $\rho_w = \frac{\dot{M}_w}{4\pi r_0^2 v_w}$ is the stellar wind density at the distance r_0 and $\rho_a = n_a \mu$ is the density of the ambient medium. The corresponding number densities are n_w and n_a . Where the stellar wind and ambient medium collide near head-on, the ram pressures are much greater than the gas thermal pressure, thus the standoff distance can be expressed as:

$$r_0 = \sqrt{\frac{\dot{M}_w v_w}{4\pi \rho_a v_*^2}} \quad (2)$$

by neglecting gas thermal pressure (Wilkin 1996). The gas pressure becomes non-negligible far downstream from the star where the shell surface is roughly parallel to the stellar motion, resulting in reduced ram pressure from the ambient medium.

For physical and mathematical simplicity, most models assume that the stellar wind and ambient medium material are well-coupled inside the shock region, and radiative cooling is very efficient on the time scale of the ionized gas recombination time. The resulting shell is “momentum supported”, rather than “energy supported”, and relatively thin compared to its scale. Mass and momentum are conserved and transported within the shell. This momentum conserving assumption provides the possibility of investigating the kinematics analytically. Wilkin (1996) derived the formula for the shell’s shape by applying mass and momentum conservation and neglecting the gas thermal pressure on both sides of the shell, as well as the tangential acceleration caused by pressure gradients within the shell:

$$r(\theta) = r_0 \csc \theta \sqrt{3(1 - \theta \cot \theta)}, \quad (3)$$

where $r(0) = r_0$ is the standoff distance, and θ is the angle between the point on the shell and the apex. He also derived expressions for the surface density and the tangential velocity of the shell.

4.2. Relaxation

The analytical method has no numerical uncertainties, but necessarily leaves out some details. Once we include more terms in the momentum equation, it can no longer be integrated analytically. Assuming a bow shock is a steady state configuration, we can apply

a relaxation method to the mathematical description of the system. Using the relaxation method allows us to include more physical processes than the analytical method of Wilkin (1996), while being easier to formulate and less time-consuming to calculate than a full hydrodynamic approach.

We assumed a cylindrically symmetric bow shock shaped as an approximately paraboloidal shell. A grid with fixed angular size is created on the surface of the shell and each cell has the same angular size along both the azimuthal and the polar directions, $\delta\theta = \delta\phi = 0.5^\circ$. Due to the symmetry of such a geometry, we only need to calculate quantities in one strip of cells along the polar direction. We assume that the gas in a cell moves as a single fluid. That is, we assume rapid cooling behind the shock where the ambient and stellar wind material mix and form a uniform shell, and we neglect shear motion between front and back sides of a cell. Mass flow, gas velocity, and position calculated from the analytical formula (Wilkin 1996) are assigned to each cell as initial conditions (which were shown not to affect the results). Then, we let the program iteratively adjust these parameters by applying mass and momentum conservation.

During relaxation, the physical and geometric properties of each cell are recalculated to replace the previous values in each step until the whole system achieves convergence. In each step, the mass flow from one cell (i) into a neighboring cell (i+1) is given by:

$$\delta m^i = \delta m^{i-1} + \delta m_w^i + \delta m_a^i \quad (4)$$

where δm^{i-1} is the mass flowing out of the previous cell. The mass flows from the stellar wind and the ambient medium are δm_w^i and δm_a^i . They are given by:

$$\delta m_w^i = \frac{\delta\Omega}{4\pi} \dot{M}_w \tau \quad (5)$$

$$\delta m_a^i = -\rho_a (\mathbf{v}_a \cdot \mathbf{S}^i) \tau \quad (6)$$

$\delta\Omega$ is the solid angle subtended by the cell element, \dot{M}_w is the mass loss rate of the stellar wind, \mathbf{S}^i is the outward pointing normal vector with magnitude equal the surface area of the cell i , \mathbf{v}_a is the velocity vector of the ambient material, and τ is the time step of the iteration. Under the same condition, we also have the formula for total momentum flow from the cell:

$$\delta \mathbf{p}^i = \delta \mathbf{p}^{i-1} + \delta m_w^i \mathbf{v}_w^i + \delta m_a^i \mathbf{v}_a^i + (P_w^i - P_a^i) \mathbf{S}^i \tau + \Phi_P \quad (7)$$

where P_a^i and P_w^i are the gas pressures of the external media. The orientation of the normal is perpendicular to the direction of tangential velocity, $\mathbf{v}^i = \delta \mathbf{p}^i / \delta m^i$. Φ_P is the extra pressure term resulting from the tangential pressure gradient inside the shell. We include it in the relaxation calculation after testing our model for the case without pressure acceleration. The

distance of the cell from the star is calculated from the law of sines:

$$r^{i+1} = \frac{\sin(\beta^i)}{\sin(\beta^i - \delta\theta)} r^i, \quad (8)$$

where $\delta\theta$ is the angular separation between cells and β is the angle formed by the radius and the velocity vector. Because we assumed that the system will eventually reach a steady state, we did not try to solve a non-steady problem. Our calculation simply proceeds and finds a converging solution.

The shape of the shell and the tangential velocity along the shell, calculated by the relaxation method neglecting the contribution of the gas pressure gradient, are shown (dashed line) in Fig. 5. For this illustration, we set the star’s speed equal to 20 km s⁻¹. For comparison, the analytical solution (Wilkin 1996) is also shown (dotted line). We also show an overall shape of the calculated shell in Fig. 6. In this later calculation, we include gas thermal pressure contributions from both sides of the shell by assuming a temperature of 50K for the ambient medium and 10⁴K for the free flowing stellar wind, which gives a more accurate but only slightly different solution for the tail portion of the shell than the analytical solution. We can see that the discrepancy between our iterated result and the analytical solution (Wilkin 1996) is smaller before we add pressure acceleration to the relaxation solution. Calculations show that, in the rest frame of the star, gas starts to move with zero tangential speed from the apex of the paraboloidal like shell and accelerates until it reaches the star’s travelling speed, 20 km s⁻¹, at the end of the shell. This acceleration is due to the accumulation of mass and momentum, which are provided by swept-up ambient material and the stellar wind. In later sections, we will show that this simple picture may not be totally correct since the effect of the pressure gradient within the shell can be significant.

Fig. 5 also shows the surface density and the particle number density along the shell. The surface density increases, almost linearly, from its value at the apex of the shell. The particle number density, derived from the shape of the shell and the normal pressure components, drops rapidly from its value at the apex. It drops by a factor of four by the position where the shell passes the star. In steady state, gas in the shell should be in approximate pressure equilibrium with the average of the normal components of the pressures on the two sides. The difference between the two normal components causes a pressure gradient across the shell which causes its centripetal acceleration. From the pressure in the ionized gas, we can calculate the density: $n = \frac{P_{ram\perp} + P_{gas}}{kT}$, where we take the ionized shell’s temperature as 10⁴K.

4.3. Pressure Gradient Acceleration

Most existing solutions, both analytical (Wilkin 1996) and numerical (Mac Low et al. 1991), neglect the effect of the gas pressure gradient along the compressed shell. The exception is Comeron & Kaper (1998), who make a numerical hydrodynamic calculation, but concentrate on the case of a runaway O star moving through the diffuse ISM. In addition to the centripetal acceleration caused by the unbalanced external pressures, the variation in the pressure along the shell results in a pressure gradient that accelerates the gas along the shell. The momentum deposited in a cell by this effect is given by:

$$\Phi_P = \frac{P^{i-1} - P^{i+1}}{2} A^i \tau = \nabla P^i V^i \tau \quad (9)$$

Where P^i and ∇P^i are the pressure and the pressure gradient in the i th cell. A^i and V^i are the cross section and the volume of the cell. We derive the thickness of each cell from the emission measure, using the ionization-recombination equilibrium equation, and the density, calculated from the balance between gas pressure and ram pressure assuming stellar parameters appropriate for G29.96 (section 4.4.1). We then assume that the thickness of the given cell is constant. If the central star is unable to ionize the whole shell, the thickness of the shell is slightly greater than that of the ionized layer, with the neutral gas in a thin, dense region just outside of the HII region. The thickness increases from the apex of the shell to the tail region because the density drops along the shell. The results of the relaxation are shown with a solid line in Fig. 5. The analytical solution is shown as a dotted line for comparison.

From the plots in Fig. 5, we can see that the change to the shape of the shell caused by including the pressure gradient is very small. Thus the change in the ionized gas number density is also small, because it is calculated from the ram pressure normal component, which directly relates to the shape of the shell. In the region close to the apex, this change can be neglected. A larger change is seen in the tangential velocity plot. For the parameters assumed, which includes a partially ionized shell, the velocity near the head of the bow shock increases so that the gas speed is $\sim 1 \text{ km s}^{-1}$ higher than without the pressure gradient acceleration at $\theta \sim 1 \text{ radian}$. Without the pressure gradient, the maximum velocity that gas can achieve is the speed of the star. With the additional acceleration provided by the pressure gradient, the gas in the shell can reach higher velocities. The tangential speed finally drops as the shell picks up more mass from the ambient medium and the pressure gradient acceleration effect decreases toward the end of the shell due to the drop of stellar wind ram pressure. With the parameters we have chosen, the maximum speed that gas can achieve under the pressure gradient acceleration is 1.3 km s^{-1} higher than the speed of the star. Up to this point, we have assumed that the ionized gas and the swept-up neutral gas

are coupled, so they share the momentum carried by the stellar wind and ambient medium. When including the effect of a pressure gradient, we assume that the force resulting from this effect is also shared by ionized and neutral gases. In fact, most of this force should be exerted on the ionized gas only, since a pressure gradient causes a force per unit volume and the ionized gas fills most of the volume. If the ionized gas can slip past the neutral layer, it should reach a higher velocity than what we present in this work. The resulting speed should be similar to that in a fully ionized shell situation.

If the optical depth of the shell is small for ionizing radiation, the ionizing photons will ionize the whole shell or penetrate the shell and ionize the ambient medium beyond it. In this “ionizing photon leaking” situation, the pressure gradient acceleration effect will reach its maximum because the force is proportional to the thickness of the ionized shell. Our calculations show that the gas speed in the shell can reach 1.25 times the star speed in the range 10 - 20 km s^{-1} , and there is no drop in speed for angles larger than 2.4 radians seen in Fig. 5(b).

In this work, we only show the results of the single layer bow shock model. Including multiple layers to our model is a logical next step. Furthermore, we leave out the pressure gradient in the hot post-shock gas on the inner side of the shell from our model. Since it is so hot ($\sim 10^7$ K), it should cool very slowly. It is even harder to include the contribution from this part of HII regions in the model.

The pressure gradient accelerates gas inside the shell, thus decreasing the surface density. It does not affect our flux maps because the brightness of each cell in our model depends only on the number of ionizing photons, as long as the shell is only partially ionized. However, the change in the surface density will affect the thickness of the neutral part of the shell, thus affecting the appearance of corresponding molecular flux maps. A kinematic study of the neutral component associated with ionized bow shock structures might prove useful.

If pressure gradient acceleration is ignored, the spatial and kinematic structure of a modeled bow shock depend on two parameters: the speed of the star and the stand-off distance. The dependence of the stand-off distance on the stellar mass-loss rate, stellar wind terminal speed, stellar speed, and the ambient medium density is given in Eq. 2. As is discussed above, inclusion of the effect of the pressure gradient in the ionized gas has little effect on the spatial distribution, but changes the velocities much like an increase of the stellar speed would. A set of models for UCHII regions in G29.96 and Mon R2 is given in Table 1, where plausible values, based on other observations (see references in the table), are given for unconstrained parameters.

5. Comparison with Observations

Our relaxation models of bow shocks provide the shape of the shell and the Doppler shift at each point on the shell. We calculated the [Ne II] emission at each point on the shell, assuming ionization-recombination balance in the shell, taking into account the angle at which the ionizing radiation hits the shell. We ignore any dust that might be present in the region.

The model ionized shell was tilted relative to the line of sight to improve the agreement with the data, sampled and remapped onto the sky with a spatial grid $0.2'' \times 0.2''$, and then convolved with TEXES’s velocity resolution of 4 km s^{-1} and a model of TEXES’s beam of half-maximum radius $r \sim 0.8''$. For G29.96, we convolved with an additional turbulent linewidth of 10.0 km s^{-1} to improve the agreement with the observations. In Mon R2, we convolved the data with the the narrowest line width $\sim 8.8 \text{ km s}^{-1}$ (Jaffe et al. 2003). Our observing sampling grid is much coarser than our modeling grids in the region corresponding to our observations, so the error caused by the quantization of the modeling grids is small.

5.1. G29.96 -0.02

Four model parameters are constrained with varying uncertainties by our observations: the standoff distance (r_0), the tilt of the symmetry axis from our line-of-sight, the speed of the star relative to the ambient medium and LSR velocity of the star (or equivalently of the molecular cloud). In addition, the stellar ionizing luminosity and spectral type, and the neon abundance combine to determine the [Ne II] brightness. Other parameters, notably those from which the standoff distance can be calculated, can be determined from other observations of our objects or estimated from typical O-star properties. Parameters determined in this way are given in Table 1.

We rotate the observed flux datacube 26° (assuming p.a.= 64° , Martín-Hernández et al. 2003) counter-clockwise in order to orient the axis of the shell horizontally in the figures. We also position the observed flux map so that the position of the ionizing star matches that in our model. A cross at (0, 0) in the map (Fig. 1) indicates the position of the ionizing star. The spatial distribution of the [Ne II] emission is reproduced better if the motion of the star in the model is within 45° of the plane of the sky, but a bigger angle tends to give a better fit in position-velocity diagrams. We chose to tilt the shell 50° away from us in our model.

As discussed in section 4.3, we assume that the ionized gas and the neutral gas in the shell are moving together, and we pick parameters so that the shell is only partially ionized. A stellar speed of $v_* \sim 20 \text{ km s}^{-1}$ is picked to fit the observed range of velocities.

An LSR velocity of the star of $V_{*,LSR} = 104 \text{ km s}^{-1}$, or $V_{amb,LSR} = 89 \text{ km s}^{-1}$ is needed to fit the velocity offset observed. However, observations of the nearby molecular material (Churchwell et al. 1990; Cesaroni et al. 1992; Afflerbach et al. 1994; Olmi & Cesaroni 1999; Lumsden & Hoare 1999; Martín-Hernández et al. 2003) give $V_{amb,LSR} = 92 - 100 \text{ km s}^{-1}$, with most numbers near 98 km s^{-1} . A stellar speed of $v_* \sim 10 \text{ km s}^{-1}$ would allow better agreement between the model velocity offset and the molecular observations, but would not fit the observed [Ne II] velocity range unless the pressure gradient acceleration is larger than in our model.

The simulated [Ne II] flux map and P-V diagrams on cuts through various positions in the model are shown with corresponding diagrams from observed data in Fig. 7-8s. The accelerating, paraboloidal like flow produced in the bow shock model successfully matches many global features in the observed data. The model produces the limb brightening at the head region, although the fit would be improved by using a smaller tilt away from the observer. The curvature of the bright ridge is also fit well. Cuts perpendicular to the shell axis show similar central velocity shifts, spatial and spectral ranges, and overall shape, including a “>”, in both the observations and the model (Fig. 7). From cut to cut, the curvature of the “>” changes because the motion of the shell with the star gives more redshift to gas closer to the apex than to down-stream gas. Our line-of-sight passes through the ionized shell twice for positions near the symmetry axis. Given the orientation of the UCHII region, the far side is closer to the apex, contains higher density gas, and dominates the line emission. The near side is farther from the apex and has lower density gas. At the edges of the cuts, we also see more lower density gas. The “>” forms because gas closer to the apex is less blue-shifted, compared with gas farther from the apex. Because the cuts are perpendicular to the symmetry axis, the model P-V diagrams are necessarily symmetric. Asymmetries in the observations are also small. In cuts parallel to the symmetry axis (Fig. 8), the P-V diagrams show a “7” like pattern, with a curved leg and a rather flat top “arm”, indicating a large velocity gradient at the head and less velocity change towards the tail. The line is also broader at the head region. These are predicted by the model too. In our velocity plot (Fig. 5), we can see that more than 80% of the change in the tangential velocity happens in the first $\pi/2$ radians. The line is broader because the scale length for velocity change is smaller in the head region. The remarkable similarity of the models and the observations is a clear indication for a large-scale paraboloidal like flow in this UCHII region.

5.2. Mon R2 IRS1

Our observations of the compact HII region in Mon R2 IRS1 are presented in a previous paper (Jaffe et al. 2003). With a 24'' diameter shell and a bright southeast ridge, [Ne II] emission in Mon R2 shows complex and broad velocity structure. We speculated that we were looking at a kinematic pattern in which material flows from the bottom to the rim of a bowl-like feature. Here, we try using the bow shock model to interpret the observations, since the object also has a cometary appearance. In order to show the similarities between the kinematics of a shell-like flow structure and the observed data, we choose parameters so that the pressure gradient acceleration is negligible. The results of two models with different standoff distances are shown in Figs. 9-14. In the first model, we try to match the ionizing star position to that in near-infrared observations that are good to $< 1''$ (Yao et al. 1997). In the second model (Table 1), we use a bigger standoff distance, which gives a better fit to our [Ne II] observations. In both cases, we tilt the shell 20° toward the observer in the simulation for a good fit to the observed P-V diagrams. As in the G29.96 -0.02 case, we derive a $V_{amb,LSR}$ different from the value we found in the literature for Mon R2. An additional $\sim 8 \text{ km s}^{-1}$ redshift is needed to shift the center of the line to the value in the observational data. It is interesting to note that Mon R2 requires a redshift and is tilted toward us while G29.96 is tilted away and requires additional blueshift. This may indicate the pressure gradient may have a bigger effect on the gas acceleration than we calculate and that a more sophisticated model might fit the data with a smaller stellar velocity.

Qualitatively, the model agrees with the data. The observed morphology appears cometary, with a bright arc and a fainter tail, although the tail ends more abruptly than in the model. The P-V diagrams show two peaks over most of the region, as is expected where our line of sight passes through the front and back sides of a shell.

If the predominant motion were due to expansion of the shell, rather than flow along the surface, the velocity splitting would increase only gradually moving from the edge of the shell into the center. As in G29.96, the motions in Mon R2 are consistent with gas flow along a shell. However, there are a few facts which make Mon R2 HII region hard to fit into the bow shock model. First, there is a compact broad-lined region near or just inside of the apex of the observed shell, which is not predicted by the model. It is most apparent in Fig. 11 and Fig. 14, where it produces the central ridge in the P-V diagrams. This component is also shown in our previous paper (Jaffe et al. 2003, Fig. 7). This source may be a result of the shock front overtaking a dense clump in the molecular cloud, or, it could result from an instability in the front, as is seen in the hydrodynamic models of Comeron & Kaper (1998). The second difficulty is that a larger standoff distance is required to make the curvature of the shell the same as in the data. In the first cut of Figs. 9 and 12, where our observed

P-V diagrams only show one component, our model P-V diagrams show two components. In addition, the shell appears to be closed on the back side. The outermost contours on the images are nearly circular, although the rim is much brighter at the bottom of the map than at the top. The model predicts that the shell is always open toward the tail.

In our figures 9,10 for both the model and the data, cuts parallel to and near the shell axis show two components. At the ridge of the shell-like region, these two components are connected by a broad line with a width up to 40 km s^{-1} . The relative strengths and the separation of the two components changes with the position of cuts. Normally, the blue-shifted component is seen farther toward the tail because the tilt of the shell puts the denser part of the near side of the shell farther from the head than the far side. The single broad line in the P-V diagram of the cut made in the center of the ridge is probably caused by the additional source there.

The observed P-V diagrams of the cuts perpendicular to the shell axis (Fig. 11,14) demonstrate the gradual change of a circular structure, which is typical for cuts across a rotationally symmetric shell. If we neglect the broad-line component at the peak of the flux map, our model and observed P-V diagrams agree well. Compared to the observations, the model with a smaller standoff distance predicts a smaller spatial span (Fig. 11). Once we increase the standoff distance (Fig. 14), we no longer have this problem. A density gradient along the symmetry axis of the shell might be able to explain the curvature of the shell, although there is at present no concrete evidence for such a gradient.

6. Discussion

We have shown that the overall velocity structure behind the cometary shape of UCHII regions in G29.96 -0.02 and Mon R2 is formed when ionized gas flows along a paraboloidal like surface. Using the bow-shock model, we can reproduce this kind of structure. We found that the model provides a good qualitative explanation of our observations of G29.96 and Mon R2. Both sources have morphologies similar to that predicted by the model, at least near the apex of the shell. The observed line profiles, as seen in the P-V diagrams, are generally double-peaked, indicating that the gas is swept up into a thin shell, so each line of sight passes through two surfaces with different Doppler shifts. The two Doppler components reach a maximum separation near the shell apex, indicating that the gas accelerates along the shell, and that the dominant motion is along the shell rather than radial.

There are quantitative differences between the model and the data, especially in the case of Mon R2, as discussed above, indicating that a complete description of these sources

will have to be more complicated than our simple model. Nevertheless, we think that the bow shock model must be essentially valid. Now we consider whether this model resolves any of the problems associated with the study of UCHII regions, and how the model might be improved.

The current bow shock model assumes that the stellar wind material and the ambient medium mix well and cool efficiently after they collide, so their mass and momentum contribute to the swept-up layer and the velocity of the ionized gas is that of the single swept-up layer. However, this momentum-conserving thin shell assumption is not well justified. Behind the shock, stellar wind material is collisionally heated and ionized. This gas will have a temperature $> 10^7$ K and does not cool efficiently, keeping the layer thick. This high temperature layer forms between the stellar wind and the photonionized gas layer and makes the mass and momentum exchange between the two layers difficult. The thin shell assumption is invalid in this situation. The photonionized layer is also evaporated through conduction with the extremely hot shocked stellar wind gas, which makes predicting the kinematics more difficult. There are many instabilities which can inflate the shell to make the thin shell assumption invalid. Possible candidates include the transverse acceleration instability (TAI) (Dgani et al. 1996) caused by the acceleration of the flow normal to the surface of the shell and the non-linear thin shell instability (NTSI) (Vishniac 1994; Hueckstaedt 2003) caused directly by the collision of isothermal flows. These instabilities will disturb the shell and create sub-structures with scales comparable to the thickness of the bow shock. Under such conditions, the momentum conservation assumption will not hold.

Among the other models proposed to explain cometary UCHII regions, the champagne model is the most interesting. The model applies when a massive star is found in a region with a large density gradient, such as the edge of a dense molecular cloud. The resulting HII region will expand supersonically away from the high-density region, or simply break out of the edge of the molecular cloud and cause the ionized gas to stream out of the opening in response to a large pressure gradient. The classic champagne model without a stellar wind (Tenorio-Tagle 1979; Bodenheimer et al. 1979; Yorke et al. 1983) can explain the cometary shape of HII regions but, because the ionized gas fills up the bubble and the main pressure gradient is along the density gradient, the champagne model has difficulty accounting for limb brightening and for the line profiles observed. Adding a stellar wind to the champagne model will probably produce limb brightening (Comeron 1997). Without ram pressure of the external gas, the champagne model with a stellar wind tends to produce a bigger shell in the clouds with the same density and temperature as the clouds we investigated with the bow shock model.

The main differences between the bow shock and the champagne flow are seen in the

kinematic properties of the ionized gas (Garay & Lizano 1999). First, the bow shock model predicts that the velocity gradient is steeper in the head than in the tail, which can be seen easily in our P-V diagrams, whereas the champagne model expects the largest gradient in the tail, where the fractional pressure gradient also reaches the highest value (Comeron 1997). Second, the champagne model predicts that the line widths are broader in the tail region because the gas has higher speed there and the gas motion is less parallel, while the bow shock predicts broader line widths near the apex because the gas gains more momentum there and moves cylindrical-symmetrically along the surface (in the frame of reference of the star). Finally, ionized gas near the apex of the cometary structure is at rest with respect to the ambient molecular gas in the champagne model, whereas it moves with the star and/or the shock front in the bow shock model. In all of these respects, our observations of G29.96 and Mon R2 are in better agreement with the bow shock model.

A central problem about UCHII regions is their lifetimes. The number ratio of UCHII regions and OB stars requires that UCHII regions should have an average lifetime $\sim 20\%$ of that of OB stars (Wood & Churchwell 1989a). Any model of UCHII regions has to be able to account for this. We have observed over a dozen of UCHII regions. They all have large velocity range, usually over $\sim 20 \text{ km s}^{-1}$. In the bow shock model, the velocity range of the line is directly connected to the star speed relative to the ambient medium. If 20% of UCHII regions have a bow shock-like structure, as shown in Wood & Churchwell (1989a,b) and Kurtz et al. (1994), the same percentage of OB stars should move supersonically through molecular clouds. Although evolved OB stars can be accelerated up to 200 km s^{-1} through the association ejection or supernova explosions (Blaauw 1993) and form bow shock-like structures around them (van Buren et al. 1995; Noriega-Crespo et al. 1997; Kaper et al. 1997), high speed OB stars are rare in OB associations. The velocity dispersion of OB association is generally small, only a few km s^{-1} (Jones & Walker 1988; Tian et al. 1996). Even if the molecular gas initially made the potential a bit deeper, stellar speeds of $15 - 20 \text{ km s}^{-1}$ are extremely improbable as part of a normal distribution. Including pressure gradient acceleration helps to reduce this requirement. Our calculations suggest that the needed speed is still too high to solve the problem. This disagreement indicates that the stellar speeds may be less than in our model. Due to the simplicity, our model could underestimate the acceleration of the ionized gas along the shock front. A full hydrodynamical treatment would help determine the true effect of a pressure gradient.

We are grateful to Alan Fey and Ed Churchwell for letting us use their VLA 2 cm data (Fey et al. 1995; Wood & Churchwell 1989b). We thank Gregory Shields for help on the ionization model. We also need to thank NASA IRTF staff for their help on observations. This work was supported by NSF grant AST-0205518, NSF grant AST-0307497 and

NASA grant NNG04GG92G. Thomas Greathouse is currently supported by the Lunar and Planetary Institute, which is operated by the Universities Space Research Association under NASA CAN-NCC5-679.

REFERENCES

- Afflerbach, A., Churchwell, E., Hofner, P., & Kurtz, S. 1994, *ApJ*, 437, 697
- Araya, E., Hofner, P., Churchwell, E., & Kurtz, S. 2002, *ApJS*, 138, 63
- Beck, S. C., Lacy, J. H., Townes, C. H., Aller, L. H., Geballe, T. R., & Baas, F. 1981, *ApJ*, 249, 592
- Blaauw, A. 1993, in *ASP Conf. Ser. 35: Massive Stars: Their Lives in the Interstellar Medium*, 207
- Bodenheimer, P., Tenorio-Tagle, G., & Yorke, H. W. 1979, *ApJ*, 233, 85
- Cesaroni, R., Walmsley, C. M., & Churchwell, E. 1992, *A&A*, 256, 618
- Churchwell, E. 1990, *A&A Rev.*, 2, 79
- Churchwell, E., Walmsley, C. M., & Cesaroni, R. 1990, *A&AS*, 83, 119
- Comeron, F. 1997, *A&A*, 326, 1195
- Comeron, F. & Kaper, L. 1998, *A&A*, 338, 273
- De Pree, C. G., Wilner, D. J., Mercer, A. J., Davis, L. E., Goss, W. M., & Kurtz, S. 2004, *ApJ*, 600, 286
- Dgani, R., van Buren, D., & Noriega-Crespo, A. 1996, *ApJ*, 461, 372
- Downes, D., Winnberg, A., Goss, W. M., & Johansson, L. E. B. 1975, *A&A*, 44, 243
- Dyson, J. E., Williams, R. J. R., & Redman, M. P. 1995, *MNRAS*, 277, 700
- Fey, A. L., Gaume, R. A., Claussen, M. J., & Vrba, F. J. 1995, *ApJ*, 453, 308
- Garay, G. & Lizano, S. 1999, *PASP*, 111, 1049
- Garay, G., Reid, M. J., & Moran, J. M. 1985, *ApJ*, 289, 681
- Garay, G., Rodriguez, L. F., Moran, J. M., & Churchwell, E. 1993, *ApJ*, 418, 368

- Hanson, M. M., Luhman, K. L., & Rieke, G. H. 2002, *ApJS*, 138, 35
- Hollenbach, D., Johnstone, D., Lizano, S., & Shu, F. 1994, *ApJ*, 428, 654
- Hueckstaedt, R. M. 2003, *New Astronomy*, 8, 295
- Hughes, V. A. & Viner, M. R. 1976, *ApJ*, 204, 55
- Jaffe, D. T. & Martín-Pintado, J. 1999, *ApJ*, 520, 162
- Jaffe, D. T., Zhu, Q., Lacy, J. H., & Richter, M. 2003, *ApJ*, 596, 1053
- Jones, B. F. & Walker, M. F. 1988, *AJ*, 95, 1755
- Kaper, L., van Loon, J. T., Augusteijn, T., Goudfrooij, P., Patat, F., Waters, L. B. F. M., & Zijlstra, A. A. 1997, *ApJ*, 475, L37
- Kim, K. & Koo, B. 2001, *ApJ*, 549, 979
- Kurtz, S., Churchwell, E., & Wood, D. O. S. 1994, *ApJS*, 91, 659
- Lacy, J. H., Beck, S. C., & Geballe, T. R. 1982, *ApJ*, 255, 510
- Lacy, J. H., Richter, M. J., Greathouse, T. K., Jaffe, D. T., & Zhu, Q. 2002, *PASP*, 114, 153
- Lumsden, S. L. & Hoare, M. G. 1999, *MNRAS*, 305, 701
- Mac Low, M., van Buren, D., Wood, D. O. S., & Churchwell, E. 1991, *ApJ*, 369, 395
- Martín-Hernández, N. L., Bik, A., Kaper, L., Tielens, A. G. G. M., & Hanson, M. M. 2003, *A&A*, 405, 175
- Meyers-Rice, B. A. & Lada, C. J. 1991, *ApJ*, 368, 445
- Miralles, M. P., Rodríguez, L. F., & Scalise, E. 1994, *ApJS*, 92, 173
- Montalban, J., Bachiller, R., Martín-Pintado, J., Tafalla, M., & Gomez-Gonzalez, J. 1990, *A&A*, 233, 527
- Morisset, C., Schaerer, D., Martín-Hernández, N. L., Peeters, E., Damour, F., Baluteau, J.-P., Cox, P., & Roelfsema, P. 2002, *A&A*, 386, 558
- Noriega-Crespo, A., van Buren, D., & Dgani, R. 1997, *AJ*, 113, 780
- Olmi, L. & Cesaroni, R. 1999, *A&A*, 352, 266

- Pratap, P., Megeath, S. T., & Bergin, E. A. 1999, *ApJ*, 517, 799
- Racine, R. & van den Bergh, S. 1970, in *IAU Symp. 38: The Spiral Structure of our Galaxy*, 219
- Redman, M. P., Williams, R. J. R., & Dyson, J. E. 1996, *MNRAS*, 280, 661
- . 1998, *MNRAS*, 298, 33
- Sewilo, M., Churchwell, E., Kurtz, S., Goss, W. M., & Hofner, P. 2004, *ApJ*, 605, 285
- Takahashi, H., Matsuhara, H., Watarai, H., & Matsumoto, T. 2000, *ApJ*, 541, 779
- Tenorio-Tagle, G. 1979, *A&A*, 71, 59
- Tian, K. P., van Leeuwen, F., Zhao, J. L., & Su, C. G. 1996, *A&AS*, 118, 503
- van Buren, D. & Mac Low, M. 1992, *ApJ*, 394, 534
- van Buren, D., Mac Low, M., Wood, D. O. S., & Churchwell, E. 1990, *ApJ*, 353, 570
- van Buren, D., Noriega-Crespo, A., & Dgani, R. 1995, *AJ*, 110, 2914
- Vishniac, E. T. 1994, *ApJ*, 428, 186
- Wilkin, F. P. 1996, *ApJ*, 459, L31
- Williams, R. J. R., Dyson, J. E., & Redman, M. P. 1996, *MNRAS*, 280, 667
- Wood, D. O. S. & Churchwell, E. 1989a, *ApJ*, 340, 265
- . 1989b, *ApJS*, 69, 831
- . 1991, *ApJ*, 372, 199
- Yao, Y., Hirata, N., Ishii, M., Nagata, T., Ogawa, Y., Sato, S., Watanabe, M., & Yamashita, T. 1997, *ApJ*, 490, 281
- Yorke, H. W., Tenorio-Tagle, G., & Bodenheimer, P. 1983, *A&A*, 127, 313

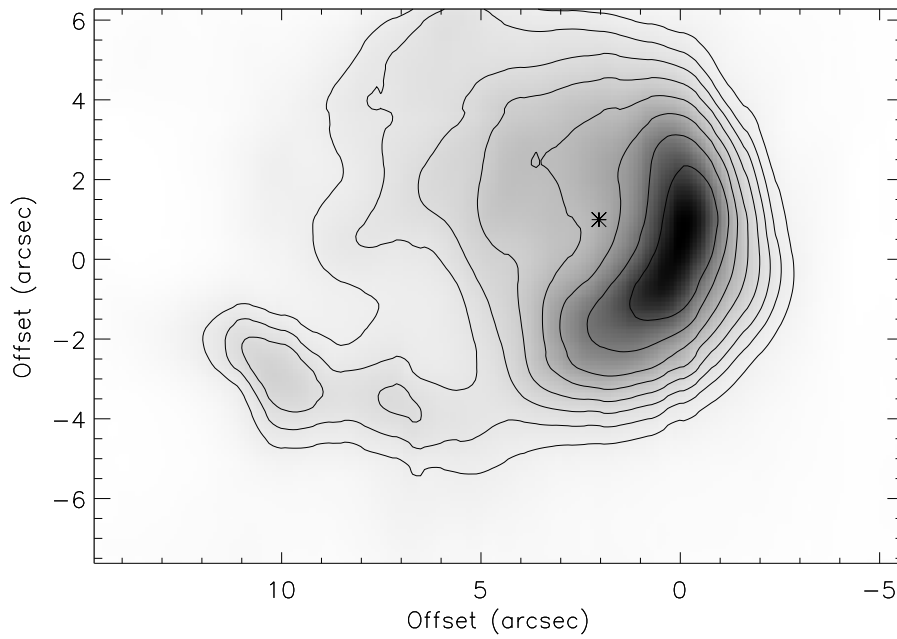


Fig. 1.— Integrated line flux map of [Ne II] line toward G29.96. The (0,0) position marks the flux peak of the observation, corresponding to $18^h46^m03^s.92, -02^\circ39'21''.9$ ($J2000$). The asterisk marks the position of the ionizing star from Martín-Hernández et al. (2003). Contours are drawn at 70%, 50%, 35%, 25%, 17.5%, 12.5%, 9% and 6% of the peak value ($1977 \text{ ergs cm}^{-2} \text{ s}^{-1} \text{ sr}^{-1} (\text{cm}^{-1})^{-1}$).

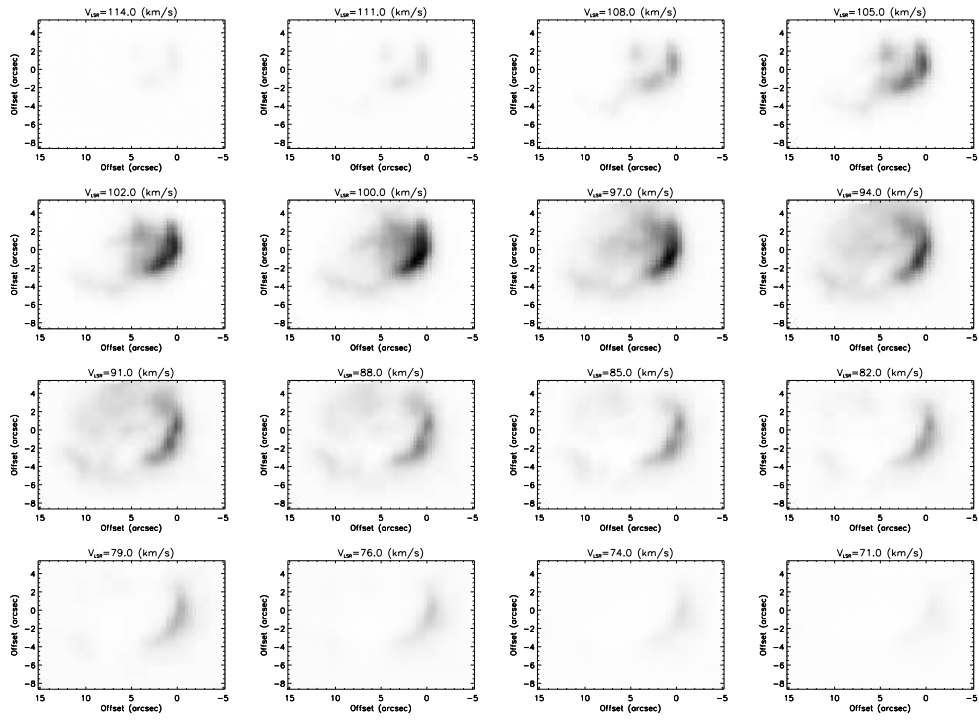


Fig. 2.— Channel maps of G29.96. Corresponding V_{LSR} is indicated in the plots.

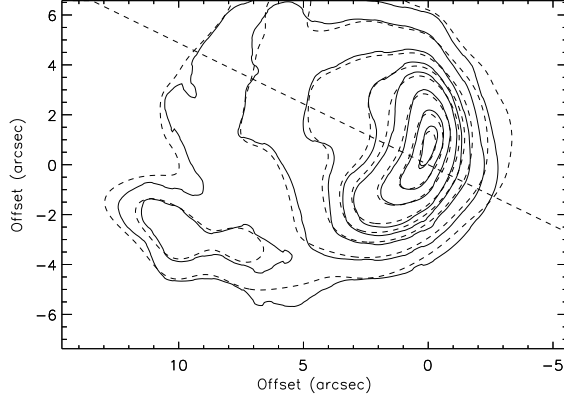


Fig. 3.— Contours of [Ne II] line map of G29.96 (solid line, peak value = $1977 \text{ erg cm}^{-2} \text{ s}^{-1} \text{ sr}^{-1} (\text{cm}^{-1})^{-1}$) overlaid on VLA 2 cm continuum observation (dotted line, peak value = 0.078 Jy/beam with a $0.56'' \times 0.49''$ beam and a 100MHz bandwidth Fey et al. 1995). The VLA map has been smoothed with the ([Ne II]) beam profile of $1.6''$ FWHM (peak value = 0.037 Jy/beam after the smoothing). Contours are plotted at 5%, 10%, 20%, 30%, 40%, 60%, 80%, 95% of the corresponding peak values. Coordinates are the offsets from the emission peak. The straight dashed line (p.a.= 64°) indicates where flux is taken for the flux distribution plot in Fig. 4.

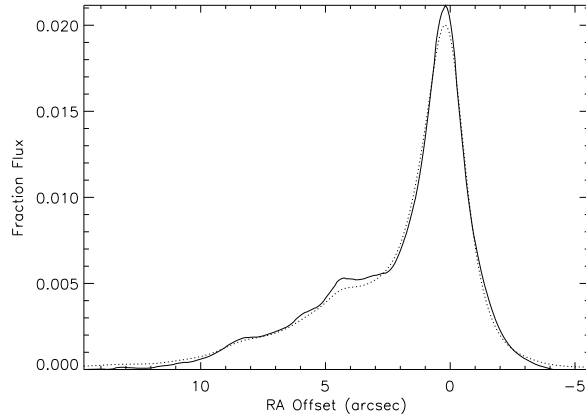


Fig. 4.— Fluxes along the symmetry axis (shown in Fig. 3 with the dashed line) of G29.96 - 0.02. The dotted line indicates the smoothed radio 2 cm flux, while the solid line indicates flux of [Ne II]. The curves are normalized to have equal integrals.

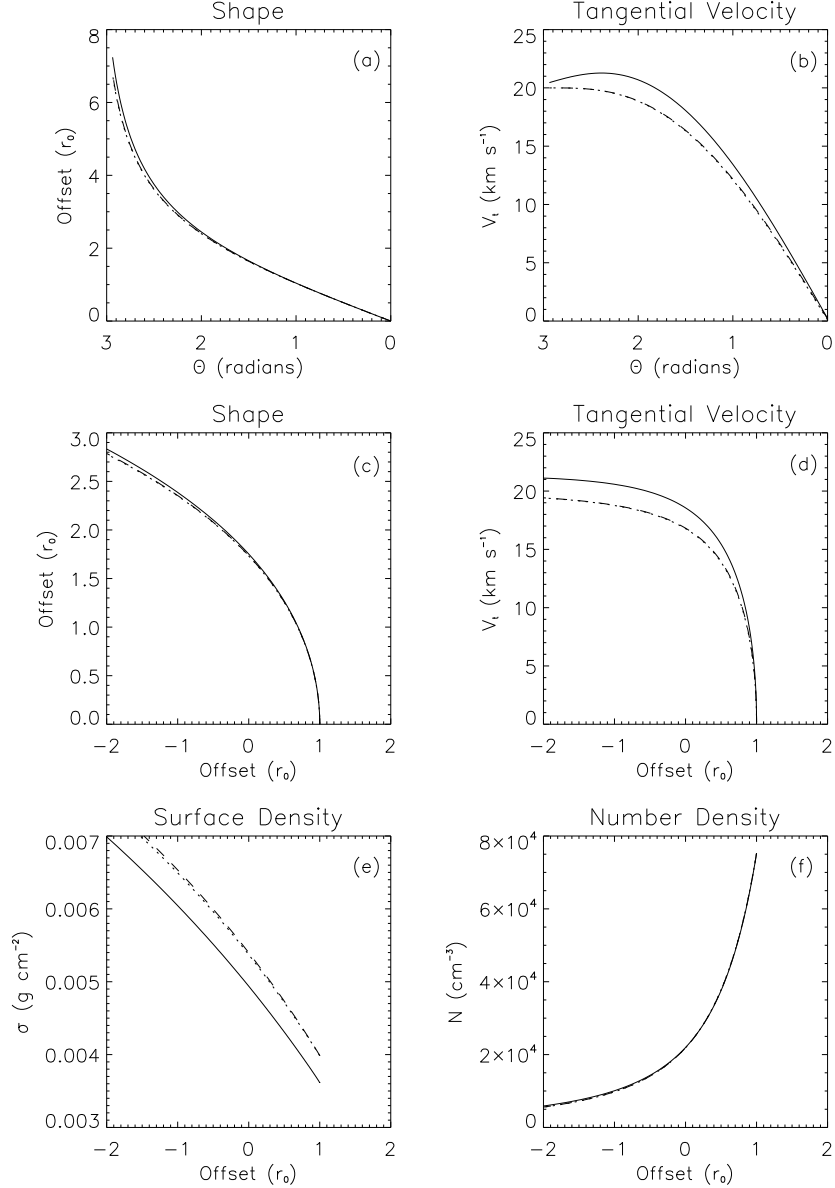


Fig. 5.— Model for G29.96 -0.02. (a) The shape of the shock, plotted against the angle from the apex (Θ). (b) The tangential velocity V_t along the surface. (c) The shape of the shock. X is the symmetry axis of the shell. Offsets are measured from the position of the ionizing star. The length unit is the standoff distance (r_0). (d) The tangential velocity V_t along the shock surface. (e) Surface density (σ). (f) The particle number density N along the bow shock. The results from Wilkin (1996) are shown with dotted lines. The model without the pressure gradient is shown with dashed lines. The model with the pressure gradient is shown with solid lines. Notice that the results of the model without the pressure gradient is extremely close to the results of Wilkin (1996).

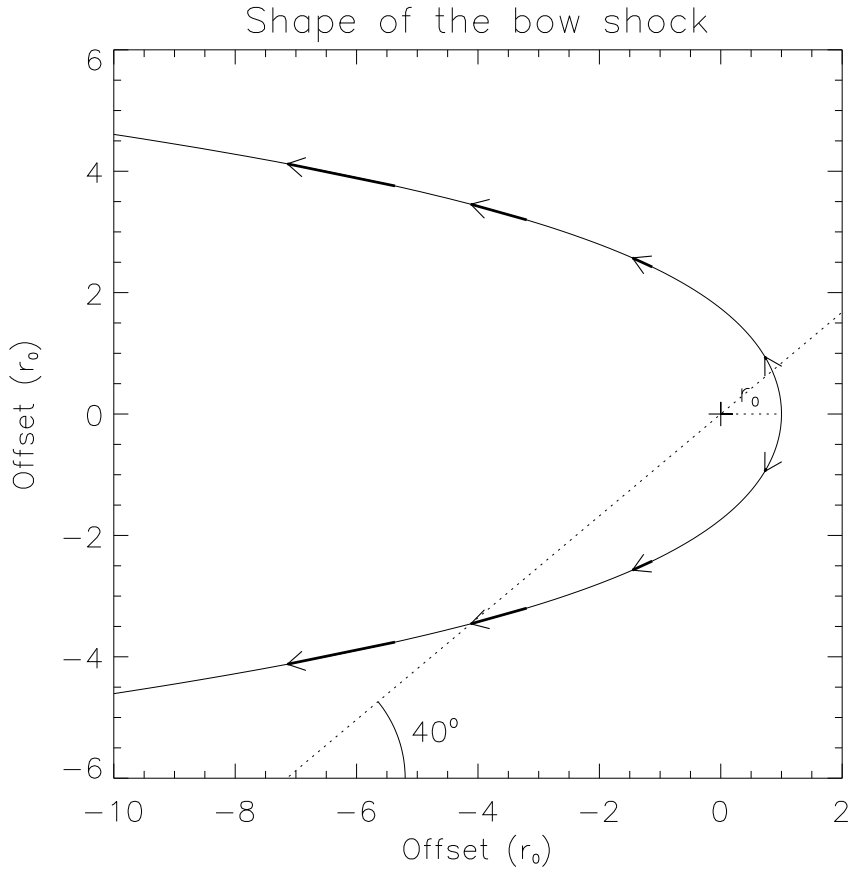


Fig. 6.— The calculated shape of the bow shock without the pressure gradient contribution and the corresponding tangential velocity vectors in G29.96 -0.02 using parameters of model 1 in Table 1. The cross at (0, 0) indicates the position of the star. r_0 , the standoff distance from the star to the apex of the shell, is the length unit in the plot. The dotted line indicates that the line of sight from the lower left to the upper right, form 40° with the symmetry axis of the shell.

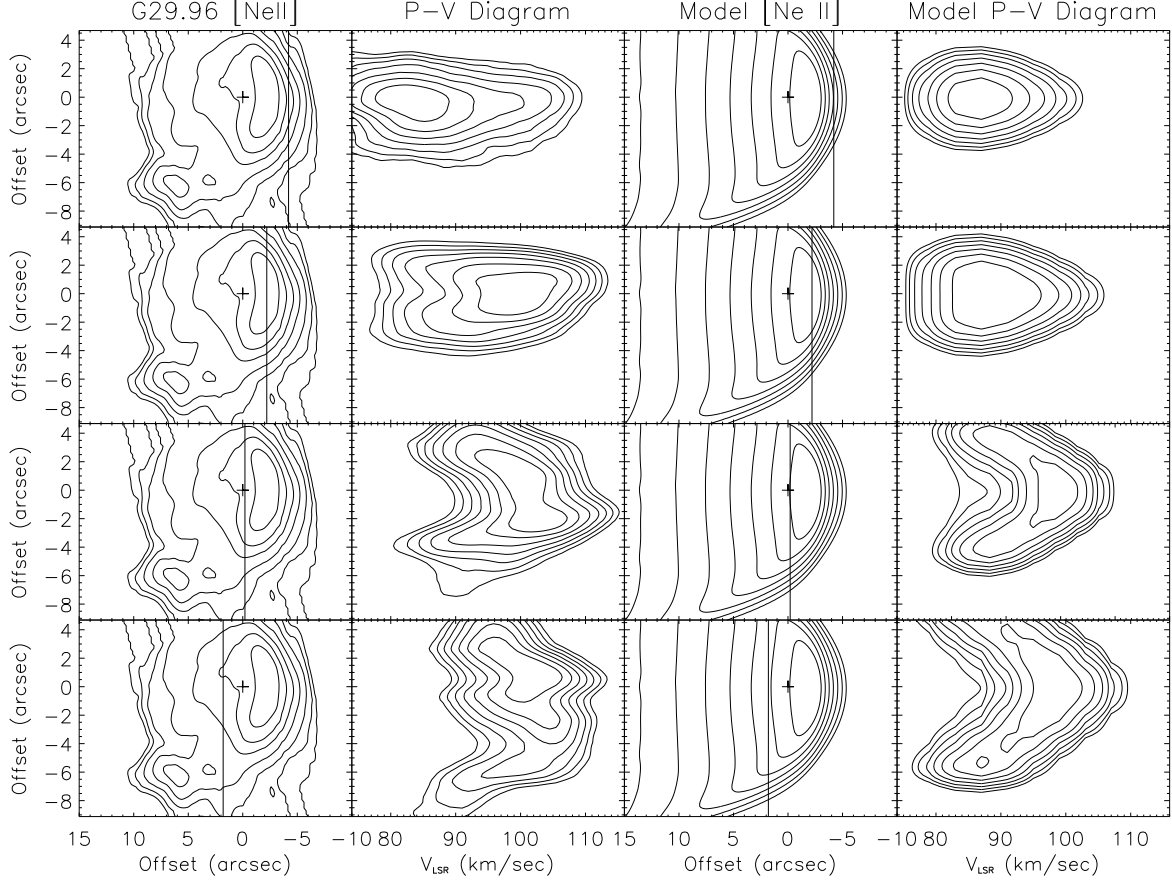


Fig. 7.— Position-Velocity (P-V) diagram of G29.96 -0.02 [Ne II] observation and that of model 1 (Table 1). Contours in the flux map are drawn at 50%, 25%, 12.5%, 6.25%, 3.12%, 1.56% and 0.78% of the peak value. Contours in the P-V diagrams are drawn in the similar way, but with contour levels separated by $\sqrt{2}$. A cross at (0, 0) indicates the location of the star according to the model. Same for the following plots.

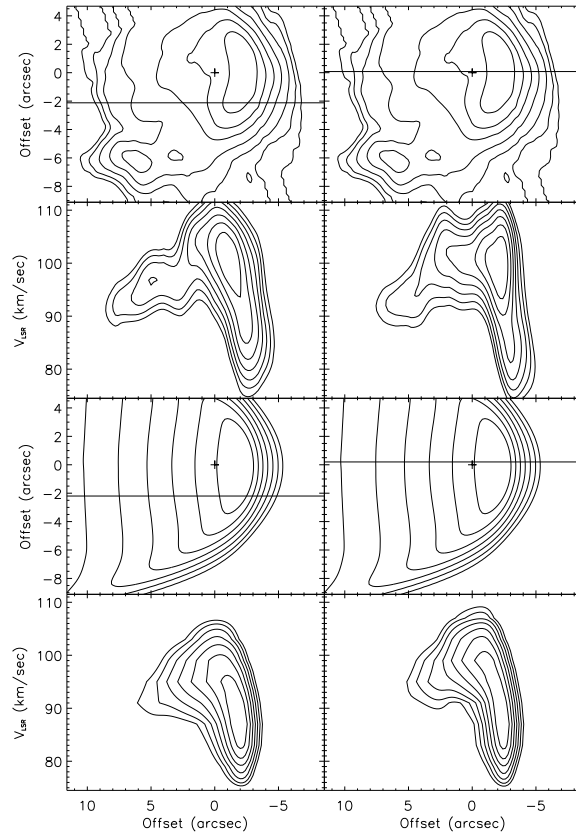


Fig. 8.— Position-velocity diagram of G29.96 -0.02 [Ne II] observation (top panel) and model 1 (bottom panel).

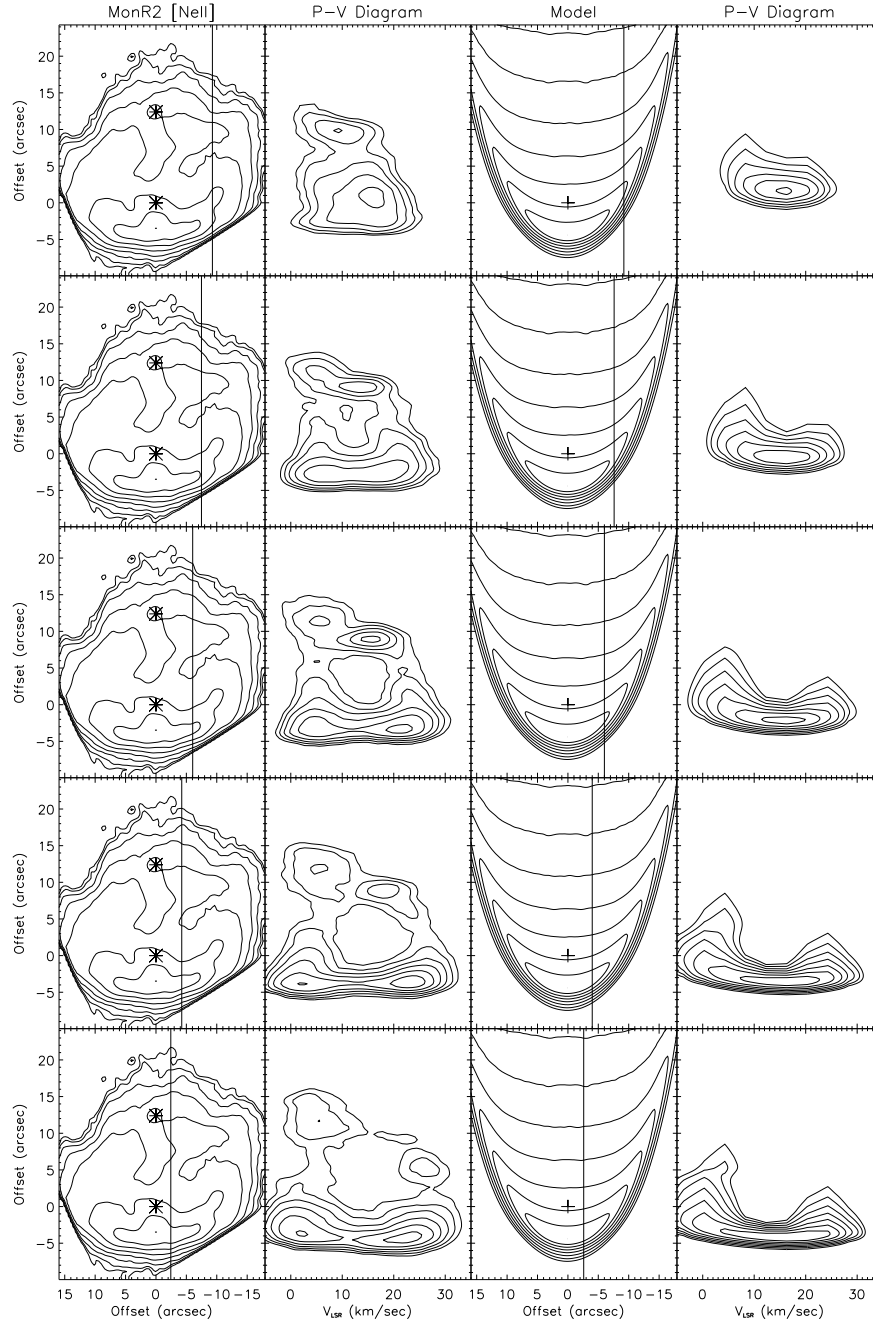


Fig. 9.— UCHII region in Monoceros R2 and model 2 with the standoff distance matching that in Yao et al. (1997) (Table 1). [Ne II] map and the position-velocity diagrams along the corresponding cutting lines. Two asterisks and one cross mark the position of IRS1 (0, 0) and IRS2 (0, 12.4) from Yao et al. (1997) and the position of the ionizing star (0, 0) used in the model.

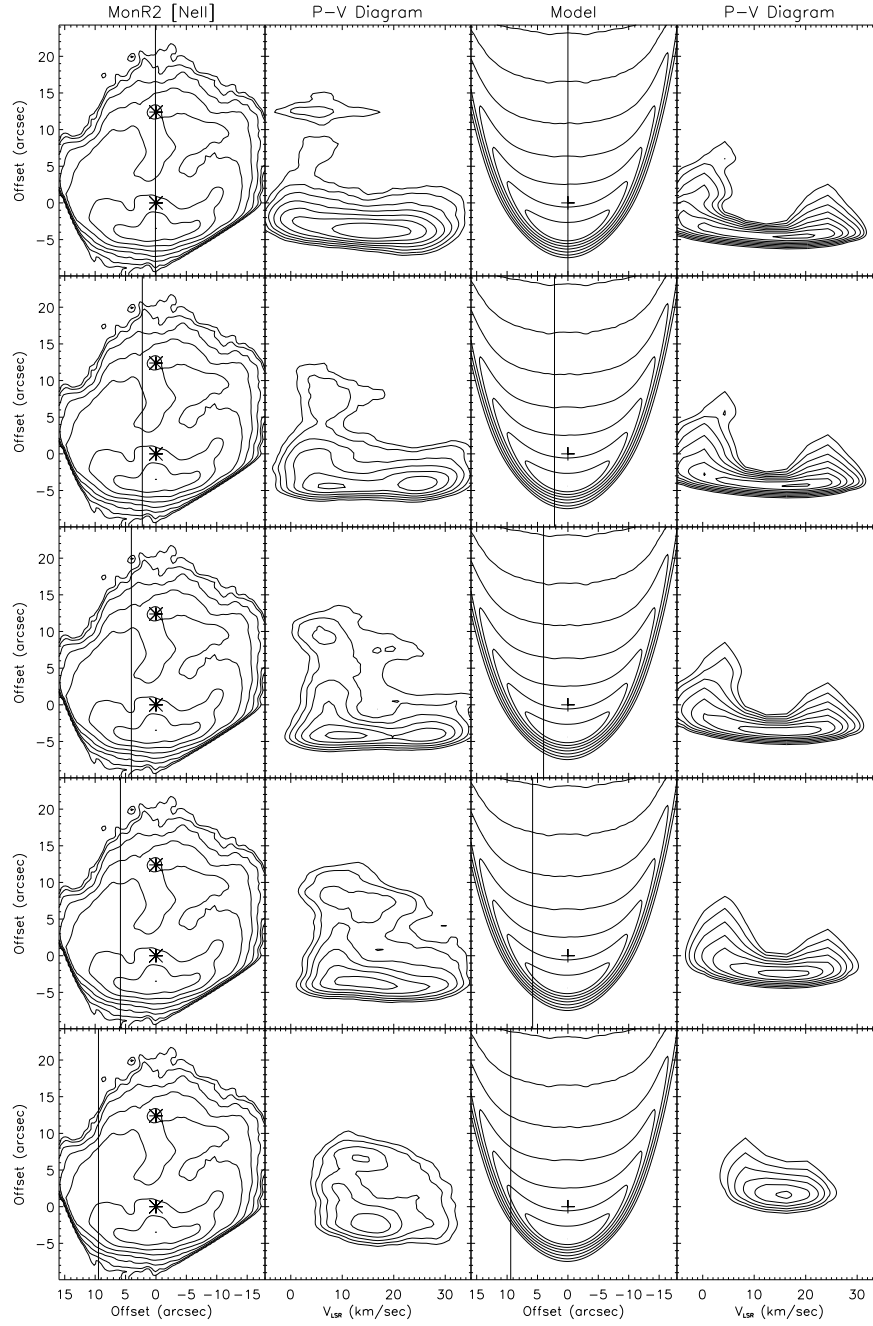


Fig. 10.— Same as in Fig. 9.

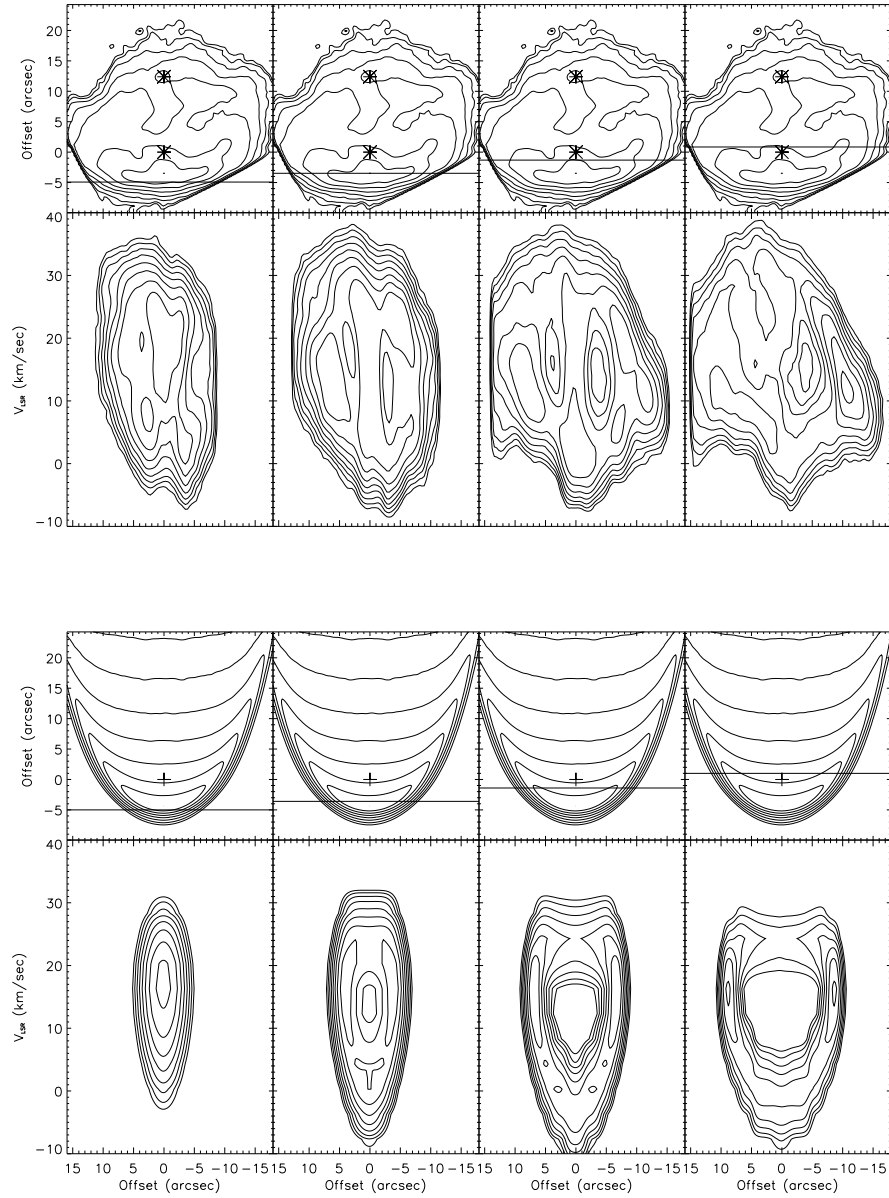


Fig. 11.— Same as in Fig. 9.

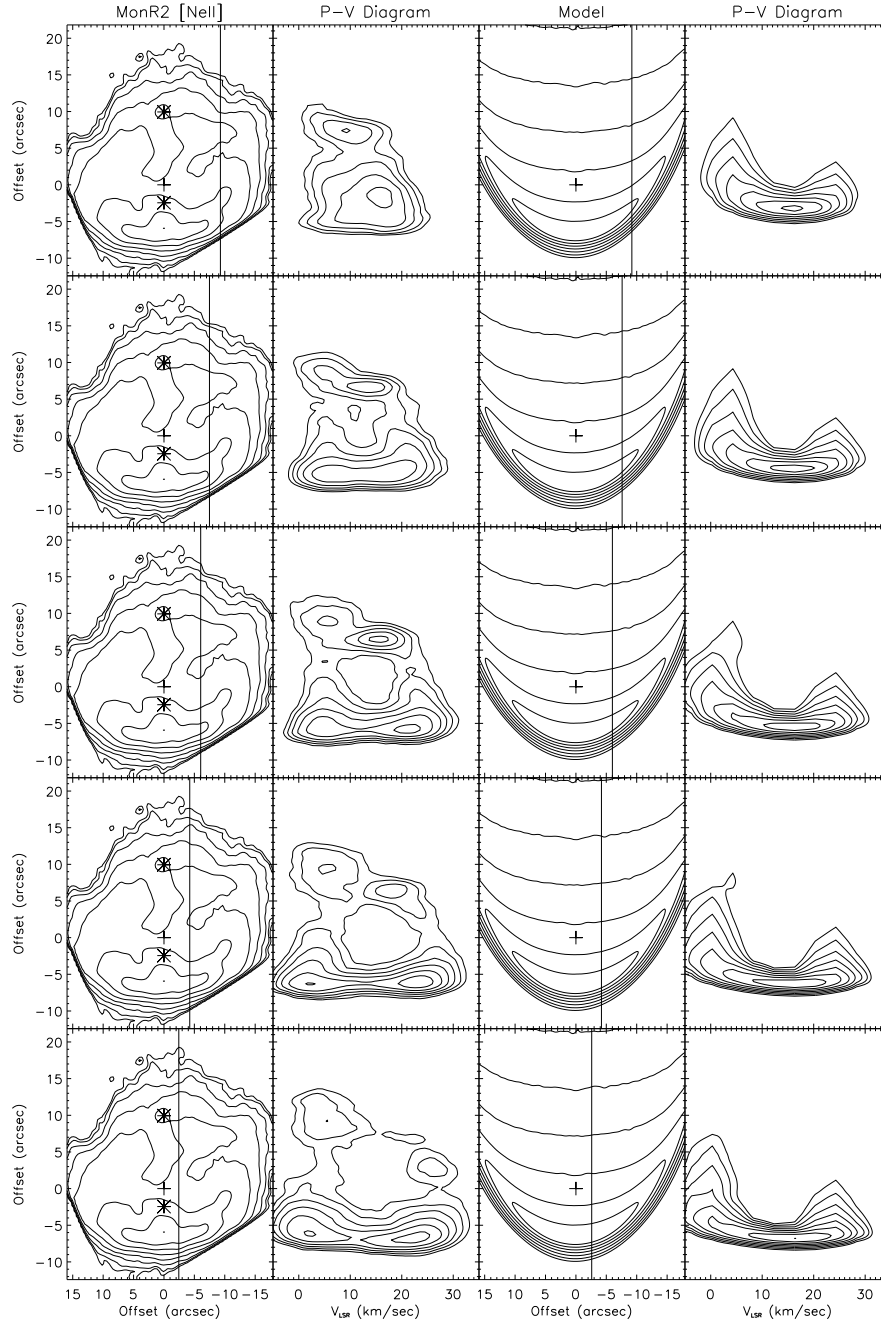


Fig. 12.— HII region in Monoceros R2 and model 3 with a longer standoff distance than that in Yao et al. (1997) (Table 1). [Ne II] map and the position-velocity diagrams along the corresponding cutting lines. Two asterisks and one cross mark the position of IRS1 (0, -2.45) and IRS2 (0, 14.8) from Yao et al. (1997) and the position of an ionizing star (0, 0) according to the model.

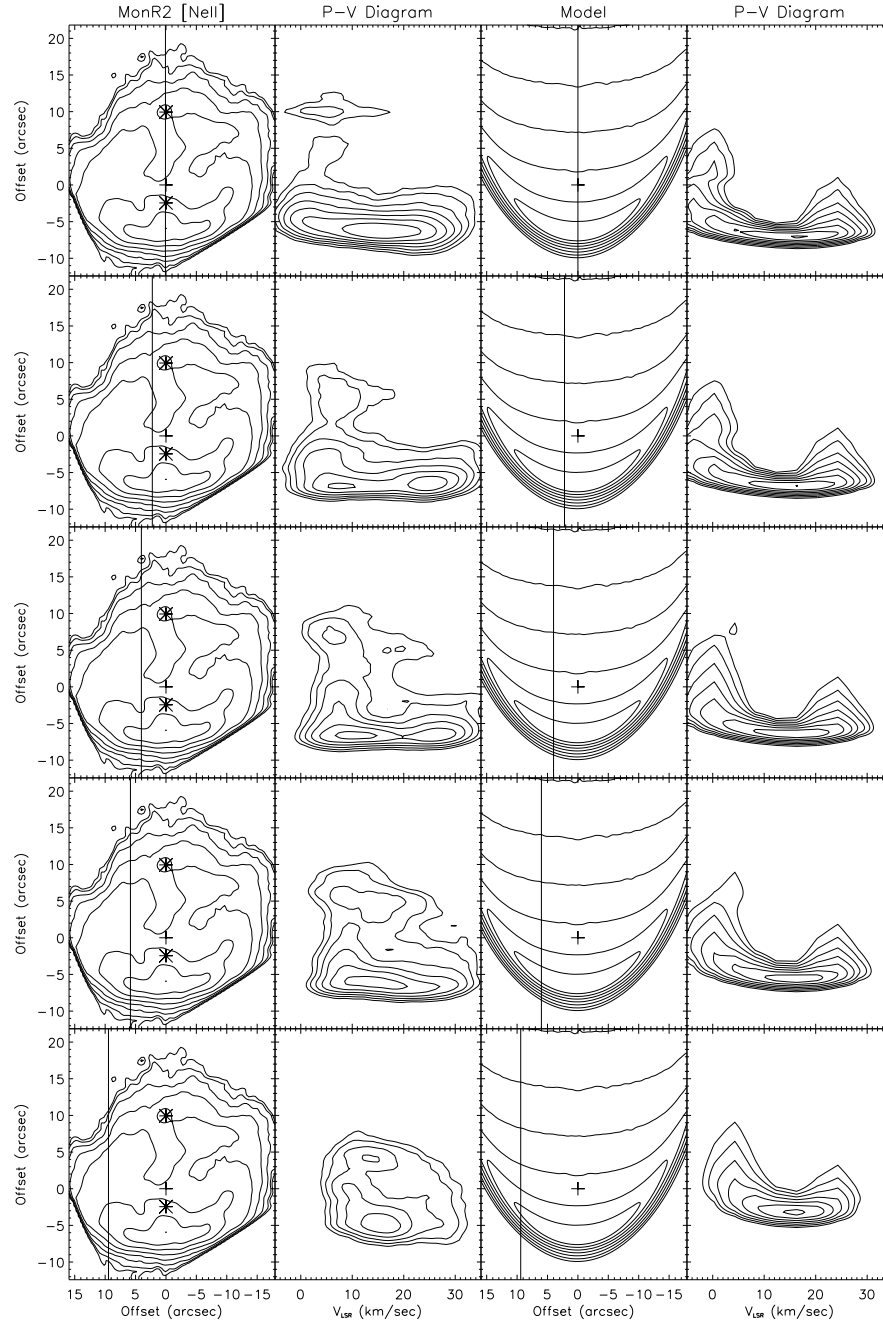


Fig. 13.— Same as in Fig. 12.

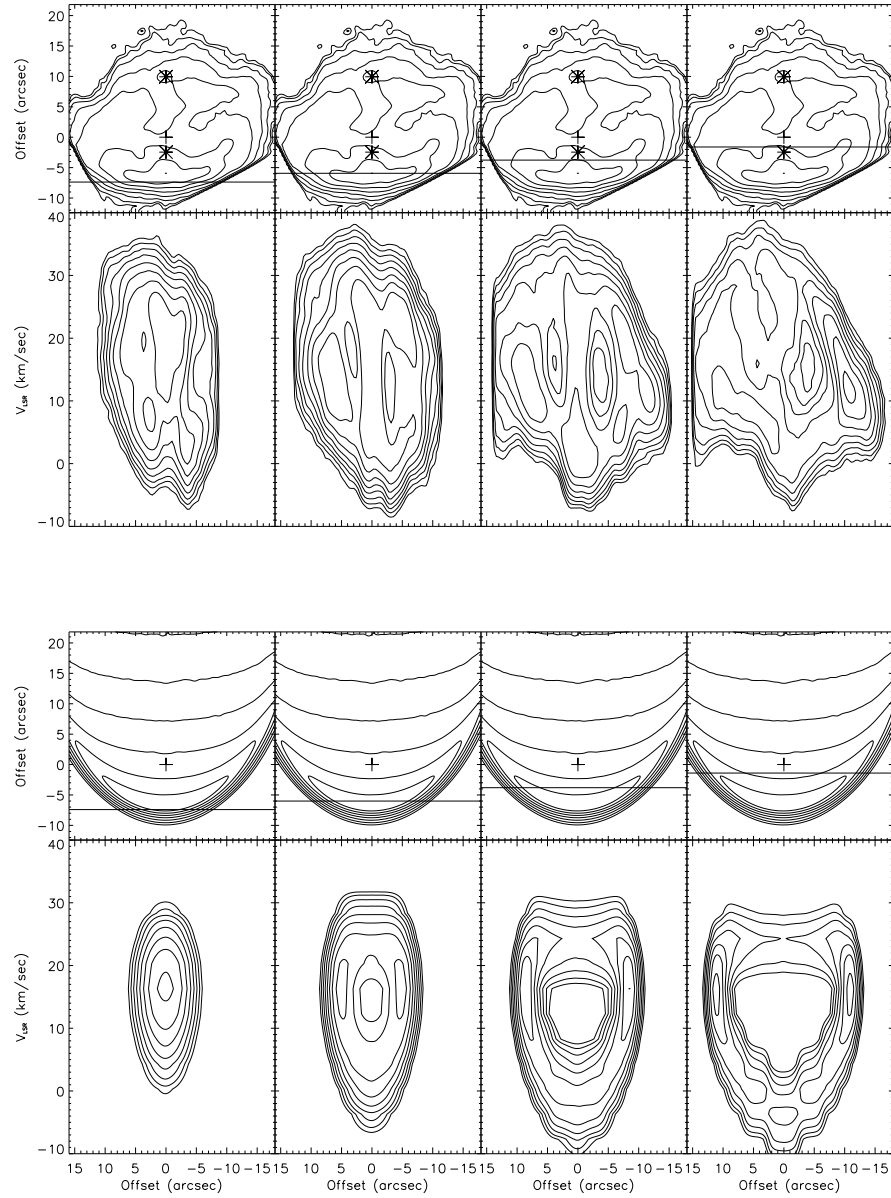


Fig. 14.— Same as in Fig. 12.

Table 1. Bow Shock Model parameters

Object Name	Spectral Type	Object Distance	Cloud Radial Velocity	Ambient Medium Density	Stellar Mass loss Rate	Stellar Wind Speed	Stellar Travelling speed	Standoff Distance	Size On The Sky	Tilt Angle
		D (kpc)	V_{LSR} (km s ⁻¹)	n_a (10 ⁵ cm ⁻³)	\dot{M}_w (10 ⁻⁶ M_\odot yr ⁻¹)	v_w (km s ⁻¹)	v_a (km s ⁻¹)	r_0 (10 ¹⁶ cm)		
G29.96 -0.02	O6 ^a	6 ^a	98 ^b	0.5 ^c	-	-	-	-	2.27'' ^d	
Model 1	O5.5	6	89	0.11	8.0	1000	20	19.6	2.2''	50°
Mon R2 IRS1	O9 ^e	0.95 ^f	10.3 ^g	0.3 ^h	-	-	-	-	4.35'' ⁱ	
Model 2	B0	0.95	10.3	0.244	3.6	1000	27	6.61	4.4''	-20°
Model 3	B0	0.95	10.3	0.238	8.0	1000	27	9.95	6.8''	-20°

Note. — We estimated the spectral type of the central star for our models from our [Ne II] line luminosity, assuming optically thin in the whole region. Free parameters of our models are the cloud LSR velocity (V_{LSR}), the ambient medium density (n_a), the stellar mass loss rate (\dot{M}_w), the stellar wind speed (v_w), the stellar speed relative to the ambient medium (v_a) and the tilt angle. For models, the size on the sky is the distance from the emission peak to the ionizing star after the tilting and the beam convolution. Positive tilt angles represent tilting the symmetry axis away from the observers. The parameters are chosen so that the pressure gradient acceleration effect is negligible.

^aPratap et al. (1999)

^bAfflerbach et al. (1994)

^cMorisset et al. (2002)

^dMartín-Hernández et al. (2003)

^eDownes et al. (1975)

^fRacine & van den Bergh (1970)

^gMeyers-Rice & Lada (1991)

^hMontalban et al. (1990)

ⁱYao et al. (1997)